RESEARCH ARTICLE

Key Points:
- The variability of shallow cumulus mass flux is observed at Barbados
- The nonprecipitating cumuli are active and contain large coherent updraft structures
- Part of the cumulus mass flux variability relates to environmental humidity

Correspondence to:
K. Lamer,
katia.lamer@mail.mcgill.ca

Observations of the variability of shallow trade wind cumulus cloudiness and mass flux

K. Lamer[1], P. Kollias[1], and L. Nuijens[2]

[1]Department of Atmospheric and Oceanic Sciences, McGill University, Montreal, Canada, [2]Max Planck Institute for Meteorology, Hamburg, Germany

Abstract Two years of ground-based remote sensing observations are used to study the vertical structure of marine cumulus near the island of Barbados, including their cloud fraction and mass flux profile. Daily radar derived cloud fraction profiles peak at different height levels depending on the depth of the cumuli and thus the extent to which they precipitate. Nonprecipitating cumuli have a peak cloud fraction of about 5% near mean cloud base (700 m), whereas precipitating cumuli tend to have a peak of only 2% near cloud base. Nineteen percent of the precipitating cumuli are accompanied by large cloud fractions near the detrainment level of cumulus tops (~1700 m). Day-to-day variations in cloud fraction near cloud base are modest (~3%). Nonprecipitating cumuli have their largest reflectivities near cloud top and an ascending core surrounded by a subsiding shell. Precipitating cumuli with enhanced elevated cloudiness (stratiform outflow) are deeper and contain larger vertical gradients in reflectivity and Doppler velocity than precipitating cumuli without such outflow. Bulk (3 h) statistics reveal that nonprecipitating shallow cumuli are active and organized. They contain on average 79% in-cloud updrafts with 86% of them being organized in large coherent structures contributing to a maximum updraft mass flux of 8–$36 \, \mathrm{g \, m^{-2} \, s^{-1}}$ just above cloud base. Alternatively, downdrafts contribute insignificantly to the mass flux and show little vertical and temporal variability (0–$7 \, \mathrm{g \, m^{-2} \, s^{-1}}$). Complementary Raman lidar information suggests that updraft mass flux profile slope is inversely related to environmental relative humidity.

1. Introduction

Trade wind cumuli are ubiquitous across the subtropical oceans [*Warren et al.*, 1988; *Norris*, 1998; *Eastman et al.*, 2011]. Despite their limited vertical and horizontal extent, these clouds play a fundamental role in maintaining the thermodynamic budget of the lower troposphere. By maintaining strong surface evaporation, they provide the moisture needed to fuel deep convection in the Intertropical Convergence Zone, which helps drive the Hadley cell circulation. The complex nature of these clouds and the lack of exhaustive observations complicate their adequate representation in numerical weather prediction and climate models [*Kollias and Albrecht*, 2010; *Rauber et al.*, 2007].

In large-scale models, a common approach to parameterize shallow cumulus clouds and their fluxes is the bulk mass flux (M, $\mathrm{kg \, m^{-2} \, s^{-1}}$) approach. This approach models a cloud ensemble into a one-dimensional plume and represents turbulent transport using air density (ρ, $\mathrm{kg \ m^{-3}}$), draft magnitude (w, $\mathrm{m \ s^{-1}}$), and areal coverage (a, $\mathrm{m^2}$) while considering mean environmental subsidence ($\overline{w_e}$) [*Tiedtke*, 1989].

$$M = \overline{\rho} a (w - \overline{w_e}) \tag{1}$$

The difference between the fractional entrainment rate (ε; inflow of environmental air in the cloud) and detrainment rate (δ; outflow of cloudy air into the environment) controls the vertical gradient of the mass flux ($\partial M/\partial z$) [*de Rooy and Siebesma*, 2008].

$$\frac{\partial M}{\partial z} = (\varepsilon - \delta)M \tag{2}$$

Expressions for these rates undergo active research. Physically, the mass flux needs to reach zero at cloud top. Considering situations with comparable buoyancy and vertical velocity, this calls for smaller (higher) detrainment (entrainment) rates for situations with deeper cloud layers. Moreover, these rates should take into account the environmental conditions. For example, in a more humid environment, the entrained air may lead to less evaporative cooling and subsequently slower reduction of the mass flux with height

[*de Rooy and Siebesma*, 2008]. Nevertheless, fractional entrainment and detrainment rates are often prescribed as constant [*Siebesma and Holtslag*, 1996], and only few modeling studies consider the effects of cloud layer depth and environmental humidity [*Kain and Fritsch*, 1990; *Derbyshire et al.*, 2004; *Bechtold et al.*, 2008]. Moreover, many such approaches have yet to be validated by mass flux profiles derived by observations.

Marine cloud observations are sparse due to the difficulty to capture their undisturbed properties from steady land-based platforms. Past ship-based campaigns that lasted only a few weeks collected basic information about the atmospheric column and the sea surface state (e.g., pressure, temperature, relative humidity, and horizontal wind) as well as point measurements (from aircraft) of in-cloud properties during cumulus-topped boundary layer (e.g., Barbados Oceanographic and Meteorological EXperiment (BOMEX), 1969 [*Holland and Rasmusson*, 1973]; Atlantic Trade wind EXperiment, 1969 [*Stevens et al.*, 2001]; and Rain In Cumulus over the Ocean 2005 [*Rauber et al.*, 2007]). These short campaigns lacked the vertical information required to characterize the depth and dynamics of the shallow cumulus. Nevertheless, they provided a detailed view of the tropospheric thermodynamic structure and surface fluxes and thus enabled some intercomparison studies [*Siebesma et al.*, 2003]. These data also provided basic case setups for Large Eddy Simulations (LES) studies, which contributed to an increase in our understanding of cumulus cloud processes [*Beniston and Sommeria*, 1981; *Nicholls et al.*, 1982].

Modeling studies would benefit from robust, more long-term observations of cloudiness and mass flux. The recently established island-based observing facilities at the Azores (http://www.arm.gov/sites/ena) and Barbados (http://barbados.zmaw.de/) equipped with state-of-the-art remote sensors are in a position to provide such observational data sets. Cloud radars are especially suited to study shallow cloud dynamics since they observe, with high sensitivity, hydrometers that when small enough can be used as tracers of air motion. Some important statistical features of marine cumulus clouds have emerged recently in the literature. Their cloud bases persistently coincide with the lifting condensation level (The Azores 710 ± 140 m [*Ghate et al.*, 2011]; Barbados 700 ± 150 m [*Nuijens et al.*, 2014]; and Nauru 500–600 m [*Kollias and Albrecht*, 2010]). *Kollias and Albrecht* [2010], using 649 h of cloud radar data indicated that marine clouds do not exhibit a diurnal cycle. *Nuijens et al.* [2014] using 2 years of ceilometer data in Barbados also commented on the seasonal invariance of cloud amount near cloud base, which may be attributed to a negative feedback mechanism of cumulus convection on cloudiness. Namely, cumulus convection acts to remove mass from the subcloud layer, which lowers the depth of the turbulently mixed layer and keeps mixed-layer top close to the Lifting Condensation Level (LCL). This in turn constrains the formation of cloud at that level. Variability of the Barbados cloud field therefore arises mainly from the variability in cloud further aloft, such as slanted deeper clouds and detrained cloud layers near cumulus tops.

In this study, we document the vertical and temporal variability of the Barbados trade wind cumulus cloudiness and dynamics (e.g., updraft/downdraft organization, velocity, fractional time coverage (analogous to areal coverage), and mass flux) using a 2 year record of profiling cloud radar data that contains the largest record of radar-documented marine shallow cumuli to date. In addition, we make a preliminary exploration of how cloudiness and mass flux relate to boundary layer thermodynamic structure, using a 3 month record of Raman lidar humidity and temperature retrievals. The presented work is organized as follows. Section 2 details the data processing steps mainly, data collection and quality control (section 2.1), cloud classification (section 2.2), and the influence of precipitation on the radar observable (section 2.3). Section 3 presents the external (cloud fraction, section 3.1) and internal (radar reflectivity and velocity, section 3.2) vertical structure of marine shallow cumuli. In section 4, we explore the mass flux structure of the nonprecipitating shallow cumuli. Section 5 attempts to relate some of the observe variability to environmental thermodynamics. Finally, the main findings are listed, and comparisons with literature are undertaken in section 6.

2. Data Processing

2.1. Remote Sensing Data Collection and Quality Control

The Max Planck Institute for Meteorology at Hamburg in collaboration with the Caribbean Institute for Meteorology and Hydrology and several other institutions established in April 2010 the Barbados Clouds Observatory (BCO) (B. Stevens et al., in preparation, 2014). The BCO is located on Deebles Point (13°09′45.5″, 59°25′43.5″, 30 m above sea level) on the east coast of the island and is exposed to the undisturbed trade winds.

The main data set used in this study is from the 35 GHz profiling cloud radar KATRIN (named after the deceased Katrin Lehman) during December 2011 to December 2013 (402 days; Figure 4e), which is a significantly longer marine cumulus data record than was previously found in literature [*Ghate et al.*, 2011; *Kollias and Albrecht*, 2010; *Wang and Geerts*, 2013]. KATRIN provides time-height observations of the atmospheric column with a temporal resolution of 10 s and a vertical resolution of 30 m. Shallow cumuli typically contain low amounts of liquid water content and small droplet sizes making them challenging to study using radars. *Chandra et al.* [2013] describes the challenges in detecting shallow cumulus clouds at the U.S. Department of Energy (DOE) Atmospheric Radiation Measurement (ARM) Southern Great Plains (SGP) site using the ARM profiling radars that have a sensitivity of around −50 dBZ at 1 km range [*Kollias et al.*, 2007; *Moran et al.*, 1998]. At the SGP, near half of the shallow cumuli detected by the ceilometer are not detected by the ARM profiling radar [*Chandra et al.*, 2013]. At BCO, the availability of a more sensitive radar (around −60 dBZ at 1 km), combined with the fact that marine cumuli have larger amounts of liquid water content and larger droplet sizes than their counterparts over land enables us to observe a higher fraction of shallow cumulus than is possible to do over land. *Nuijens et al.* [2014] investigated the differences in the measured total cloud fraction by the Raman lidar and the radar at BCO [*Nuijens et al.*, 2014, Table 1]. The radar reports 12.5% lower cloud fraction during a 2 month periods compared to the lidar. Here a different radar hydrometeor mask is used; thus, it is possible that the difference in the reported total cloud fraction by the lidar and the radar is even smaller.

To begging with, the KATRIN radar data are subjected to the standard real-time data processing routine developed for the suite of 35 GHz radars produced by Meteorologische Messtechnik [*Bauer-Pfundstein*, 2007]. Briefly, at each range gate, a slight variation of the *Hildebrand and Sekhon* [1974] technique determines the noise floor of the full Doppler spectrum information. Then, the radar Doppler spectrum is separated into its various peaks, if any, which are the contributions from the different targets present in the observation volume (e.g., cloud, precipitation, and clutter). The algorithm identifies and removes clutter targets using the linear depolarization ratio and Doppler velocity of each peak along with complementary temperature information from the nearest METAR station. For uncertain peaks, the information from the neighboring observations (in time-height) is used to consolidate the target classification.

Due to its proximity to the ocean and poor antenna cross channel, the KATRIN radar side lobes capture signal from oceanic waves creating clutter in its lowest range gates. The location of this clutter band varies daily from 0.3 to 0.6 km and is not well filtered during the routine processing (e.g., Figure 1b at ~0.5 km). A complementary filtering routine is applied to the radar moments to remove the sea clutter. First, the lowest 510 m of KATRIN radar data are discarded. In addition, all radar echoes that span two range gates or less (60 m) or in clusters smaller than nine pixels are removed (Figure 1c, green pixels). Because cloud base is rarely below 550 m, this procedure is not expected to eliminate real cloud echoes, but only rain shafts below the cloud base, which are not the main focus of our study.

In a recent study, *Ghate et al.* [2011] commented on the difficulty to characterize the marine boundary layer (MBL) thermodynamic structure at the coarse resolution provided by soundings (every 6 h). Here a 3 month record (December 2011 to February 2012) of Raman lidar measurements, with a pulsed laser beam at a temporal and spatial resolution of 2 min and 6 m, is used to explore the existence of relationships between environmental conditions, peak cloud fraction location, and the mass flux vertical variability. The concentration of water vapor is derived by measuring backscattered energy at the shifted Raman frequency in the ultraviolet spectral range. Furthermore, air temperature is derived by making use of the pure rotational Raman spectra technique. The profiles of humidity and temperature are only available during nighttime when there is no interference of background solar light, between 20:00 and 04:00 local time. Error estimation is derived using Poisson statistics for lidar signals on a 2 h averaging period. Data with error beyond 5% are not considered in our analysis.

2.2. Cloud Classification

The MBL clouds are isolated and categorized to subsequently investigate their relative contribution to cloud fraction, as well as their microphysical structure, as depicted by radar reflectivity, and dynamical structure, as depicted by radar Doppler velocity. After the application of the sea clutter rejection filter (section 2.1), the first hydrometeor base height (which can be either cloud, drizzle or a remaining rain shaft) and hydrometeor top height (which is typically cloud) are estimated (Figure 1c, black dots indicate bases). We use the location of
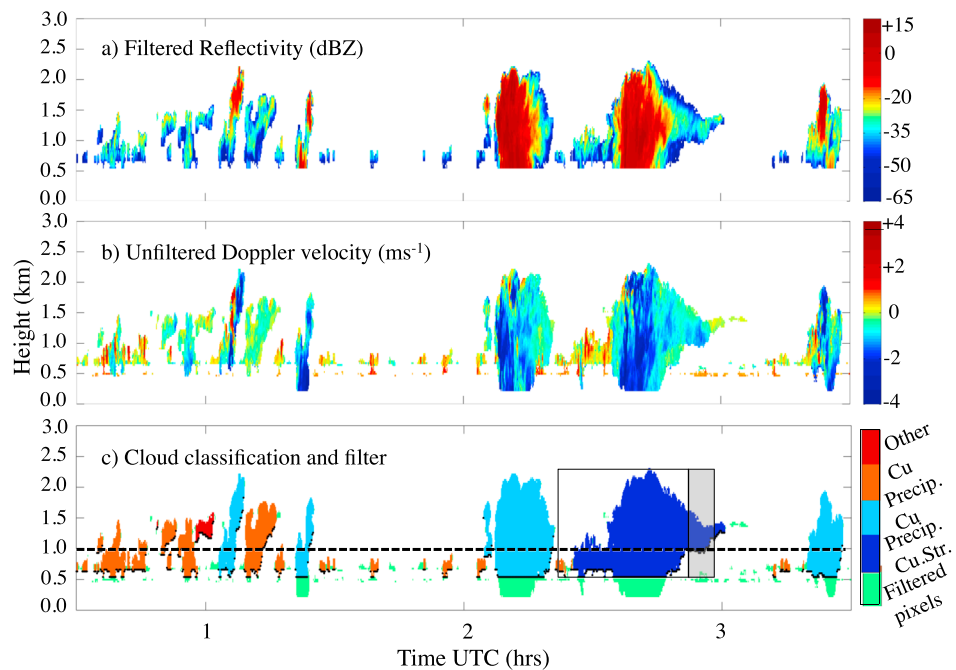
Figure 1. Three-hour period on January 27 2012 of (a) filtered reflectivity (b) unfiltered Doppler velocity (positive indicates upward motion and negative indicates downward motion) (c) cloud classification and filtered pixels (i.e., sea clutter, rain shafts, and cloud segments of negligible size) (Green: filtered pixels, red: other clouds, orange: nonprecipitating cumulus, light blue: precipitating cumulus, dark blue: precipitating cumulus with stratiform outflow). Also identified are cloud bases (black dots), a horizontal line at 1 km marking the division between the stratiform and cumulus bases, and the cumulus (clear box) and stratiform (shaded box) portion of the cumulus with stratiform outflow.

the hydrometeor base height relative to the mean LCL to determine whether a cloud is rooted in the subcloud layer and whether a significant portion of the cloud is located at heights further aloft, for instance, when the cloud is slanted or is accompanied by outflow layers near cumulus tops. Additionally, we use the duration of the hydrometeor overpasses to separate larger from smaller cloud clusters. Using those criteria, we can loosely define four categories of MBL clouds (Table 1, also illustrated in Figure 1c). First, shallow cumuli (Cu) are defined as those clouds with a hydrometeor top below 3 km and a hydrometeor base below 1 km. Hydrometeor clusters with bases between 1 and 3 km, which are clearly elevated relative to the LCL, and which last more than 2.5 min are classified as other cloud types, which may include stratiform layers, decaying cloud patches, and trailing edges of deep clouds. We also often observe cumuli that are accompanied with stratiform-like layers near cumulus tops (Cu.Str.), analogous to the clouds observed during the ATEX field experiment. These hydrometeor clusters have bases below 1 km for at least 5 min (see the cumulus segment in the clear box in Figure 1c) and additionally have bases above 1 km that last at least 2.5 min (the stratiform segment; shaded box). Finally, clouds with a hydrometeor top height above 3 km are classified as deep. The specific time duration and height threshold values used here were subjectively determined to best match our specific data set using manual inspection of the radar time-height images. All clouds can be both precipitating or nonprecipitating (classification details are in the following section).

Much of our analysis in later sections focuses on nonprecipitating clouds, for which we can adequately derive the mass flux (section 4). These clouds, colored as orange in Figure 1c, form the bulk of our cloud sample with over 40,000 clouds observed in 2 years (Table 1). It remains interesting to investigate the structure of these clouds relative to the precipitating cumulus with (Figure 1c dark blue, 617 clouds) and without upper level detrained layers (Figure 1c light blue, 2620 clouds) and investigate which mechanism leads this height shift of the location of the maximum cloud fraction.

In order to verify that our criteria properly isolate this last category (cumulus with stratiform outflow), a joint probability distribution of hydrometeor base height versus thickness, using each individual radar profile, is shown in Figure 2. The two separate panels are for the precipitating cumuli without stratiform outflow

Table 1. Cloud Type Characteristics and Occurrence

|		Cloud Types			
		Other	Cu.Str.	Cu	Deep
Hydrometeor top	Height (km)	<3	<3	<3	>3
Hydrometeor base	Height (km)	(13)	>1 and <1	<1	<3
	Duration (min)	>2.5	>2.5 and >5		
Number of clouds	Precipitating		617	2,620	
	Nonprecipitating		35	40,564	
Thickness (m)	Precipitating		$1{,}900 \pm 400^a$	$1{,}500 \pm 500$	
	Nonprecipitating		900 ± 300^a	300 ± 8	
Duration (min)	Precipitating		20 ± 20	8 ± 7	
	Nonprecipitating		8 ± 5^a	1 ± 1	
All available observations				7,170 h	
Continuous X-h periods with nonprecipitating cumulus only	3 h		1,003 periods =	3,009 h	
	2 h		1,804 periods =	3,608 h	
	1 h		4,142 periods =	4,142 h	

[a]Cumulus segment only.

(a) and those with stratiform outflow (b). The joint probability distribution function of cumulus with stratiform outflow shows two clear clusters; one comprising bases below 1 km and one comprising bases beyond 1.1 km (Figure 2b). The cluster of elevated bases shows that these layers of cloud are relatively thin. Furthermore, the thickness of these stratiform-like layers decreases with increasing cloud base height. This suggests that their depth might be limited by the presence of an inversion. One possible explanation for the presence of these thin layers is that a higher inversion height corresponds to a drier environment, because humidity generally decreases with height in the trade wind layer. This increases the potential for thin layers of cloud that form from detrained moisture near cloud tops. Overall, these cumuli are deeper than the cumuli without stratiform outflow, with hydrometeor column thicknesses ranging from 0.8 to 1.8 km. The cumuli without stratiform outflow are thinner with thicknesses ranging from 0.5 to 1.5 km. The fact that the latter class of clouds does not show the same cluster of elevated hydrometeor bases confirms that our subjective criteria produce two distinct cumulus classes. For completeness, note that the lower fraction of hydrometeor bases detected above 700 m can be attributed to thinner cloud boundaries.

2.3. The Influence of Precipitation on Radar Observables

In this section, we are concerned with the separation of precipitating and nonprecipitating clouds for which the KATRIN mean Doppler velocity can be used to retrieve the vertical air motion and estimate the cumuli updraft/downdraft magnitude, fractional coverage, and mass flux. Since cloud droplets contribute negligibly to the mean Doppler velocity (0.3 and $7 \, \text{cm s}^{-1}$ for 10 and $50 \, \mu\text{m}$ droplet, respectively; effectively an order of magnitude smaller than vertical air motion in shallow clouds), they can be used as air tracers. However, drizzle droplets and raindrops have significant sedimentation velocity (0.2 to $9 \, \text{m s}^{-1}$), which makes them poor air motion tracers [*Kollias and Albrecht*, 2010].

Techniques to identify the Doppler velocity observations that are good proxy for air motion exist in literature with various degrees of sophistication. In a statistical sense, profiling radar Doppler velocities exhibit a downward bias (negative) when precipitation size particles are in the radar volume. Most studies rely on a reflectivity threshold to determine when this happens since radar reflectivity is very sensitive to particle size. A simple reflectivity threshold may be selected (as in for example, *Frisch et al.* [1995], *Liu et al.* [2008], and *Ghate et al.* [2011]), or more sophisticated correlation between radar reflectivity and Doppler velocity may be used [*Kollias and Albrecht*, 2010; *Vali et al.*, 1998] to determine radar observations affected by nonnegligible particle fall velocities. Here we choose to avoid simple reflectivity threshold from literature since reflectivity is sensitive not only to particle size but also (to a lesser extent) to particle number concentration, which is site specific. Correlation looking for statistical departures from near zero mean Doppler velocity is not a good technique here given that we mainly sample active cumuli and as such we are expected to observe both positive (in the presence of strong in-cloud updrafts not balanced by in-cloud
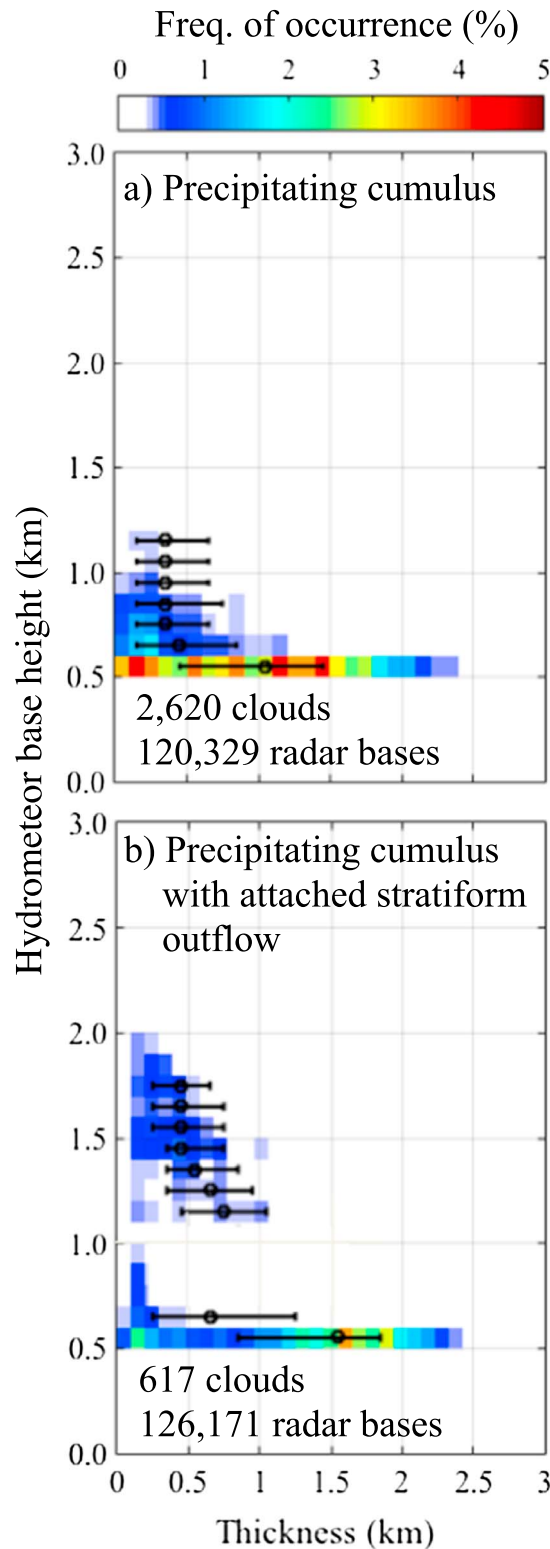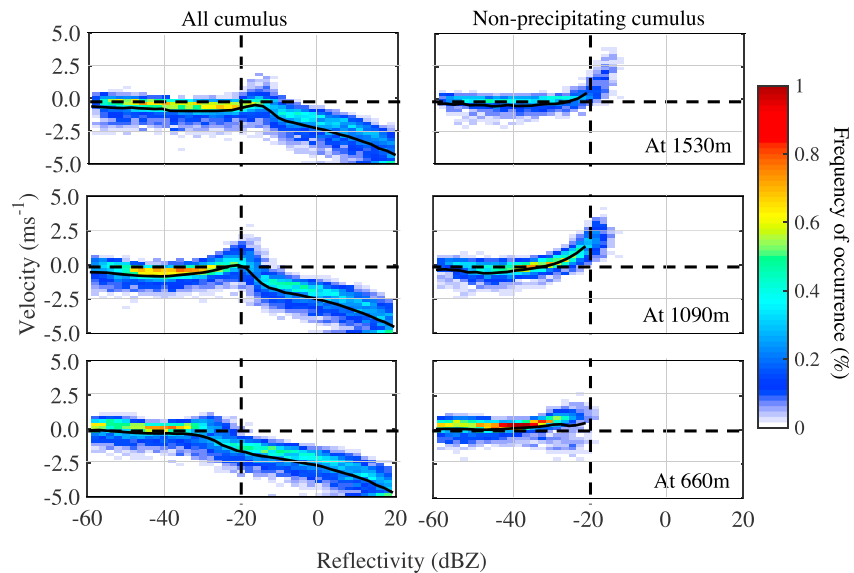
Figure 2. Joint probability distribution of thickness (bin size 100 m) and hydrometeor base height (bin size 100 m) using each individual radar profile for (a) precipitating cumulus and (b) precipitating cumulus with elevated cloud layer. The median thickness for each hydrometeor base height bin (circle) and its interquartile range (IQR, whiskers) are also included.

downdrafts) and negative (in the presence of falling particles) departures from zero mean velocity. Instead, we developed a sophisticated site-specific radar reflectivity factor versus mean Doppler velocity (*Z-V*) relationship and determined the reflectivity threshold where a systematic negative (downward) trend with increasing reflectivity is present, which is attributed to the contribution of large hydrometeor fall velocity.

An initial analysis (not shown) revealed both the expected downward trend at high-radar reflectivity (beyond -20 dBZ) and an upward trend emerges around -20 dBZ. In order to further investigate this trend, the *Z-V* relationship is reproduced for three distinct heights (660, 1090, and 1530 m) that correspond to the average height of the base, middle, and top of the cumulus clouds analyzed in this study (Figure 3, left column). At 660 m, the majority of the observed mean Doppler velocities are distributed around $0 \, \mathrm{m \, s^{-1}}$ for reflectivity lower than -30 dBZ, indicating that there is an equilibrium between the updraft and downdraft magnitudes. At 1090 m, the distribution of the mean Doppler velocities slowly shifts upward with increasing radar reflectivity. This is mostly visible in the -30 to -20 dBZ range. Section 3.2 contains a discussion about the location of each reflectivity range within individual clouds. In short, the upper centermost part of the nonprecipitating cumulus clouds contains this reflectivity range collocated with the most vigorous updrafts. At radar reflectivity higher than -20 dBZ, the particle sedimentation controls the distribution of observed mean Doppler velocities. Finally, at 1530 m, the upward trend is less pronounce since the nonprecipitating cloud population sampled decreases at the expense of the precipitating clouds.

Based on this analysis, a threshold of -20 dBZ is selected to distinguish radar echoes affected by precipitation size particles. Subsequently, a cloud containing at least four radar echoes with reflectivity above -20 dBZ and at the same time Doppler velocity below $-0.5 \, \mathrm{m \, s^{-1}}$ is considered precipitating. Similar thresholds have been proposed in the literature [e.g., *Frisch et al.*, 1995; *Liu et al.*, 2008; *Ghate et al.*, 2011]. *Kollias and Albrecht* [2010] relied on a reflectivity threshold between -22 and

Figure 3. Joint probability distribution of radar reflectivity-velocity across all cumulus observations at three levels. (left column) All cumulus clouds observed. (right column) Nonprecipitating cumulus clouds only. (bottom row) 660 m, (middle row) 1090 m, and (top row) 1530 m. The solid black line indicates the mean value. The black dashed lines show the threshold used to discriminate radar observables affected by precipitation. The total frequency of occurrence of each right panel is calculated as the number of occurrences of the nonprecipitating clouds divided by the total number of occurrence of all cumuli at the corresponding height.

−15 dBZ but removed only the precipitating segments of clouds rather than excluding entire precipitating clouds. Thus, the "precipitating cloud filter" proposed here is aggressive and may remove precipitation that has yet to leave the cloud and cannot be detected by usual ceilometer, micro rain radar, or disdrometer techniques. This, however, ensures unbiased vertical velocity statistics and prevents mass flux underestimations. Fortunately, the shear number of available clouds (tens of thousands) permits the use of a conservative nonprecipitating cloud definition without compromising the robustness of the derived statistics (Table 1). The subset of *Z-V* observations that pass through the precipitation filter is shown in Figure 3 (right column). The total frequency of occurrence of each of the panels is calculated as the number of occurrences of the nonprecipitating clouds divided by the occurrences of all-cloud observations at the corresponding height. The technique preserves the strong updrafts and eliminates the systematic downward bias caused by particle sedimentation.

3. The Vertical Structure of Marine Shallow Cumuli

3.1. Daily Hydrometeor Fraction

In this section, we measure the vertical structure of the cloud field using the hydrometeor fraction, which is the amount of hydrometeors (cloud and/or precipitation) detected relative to the entire sky (clear and cloudy/precipitating) within a day. The daily hydrometeor fraction profiles along with the interquartile ranges derived from the 2 years analyzed are shown in Figure 4. If no radar data is available (independent of the presence or absence of clouds), the data availability in Figure 4e takes a value of 0. Evidently, the radar data record contains extensive periods (from 15 days to 4 months) with no radar data. When producing Figures 4a–4d, a 3 day long running mean filter is applied to the daily hydrometeor fraction and data availability to smooth out extremes and fill data gaps in order to improve the readability of the figure.

The daily profiles of hydrometeor fraction reveal the omnipresence of MBL clouds in the lowest 3 km (Figure 4a). Deeper hydrometeor layers that extend to the top of the troposphere and cirrus clouds have a noticeable seasonal cycle with a maximum in June–November (reaching 50% occurrence) and
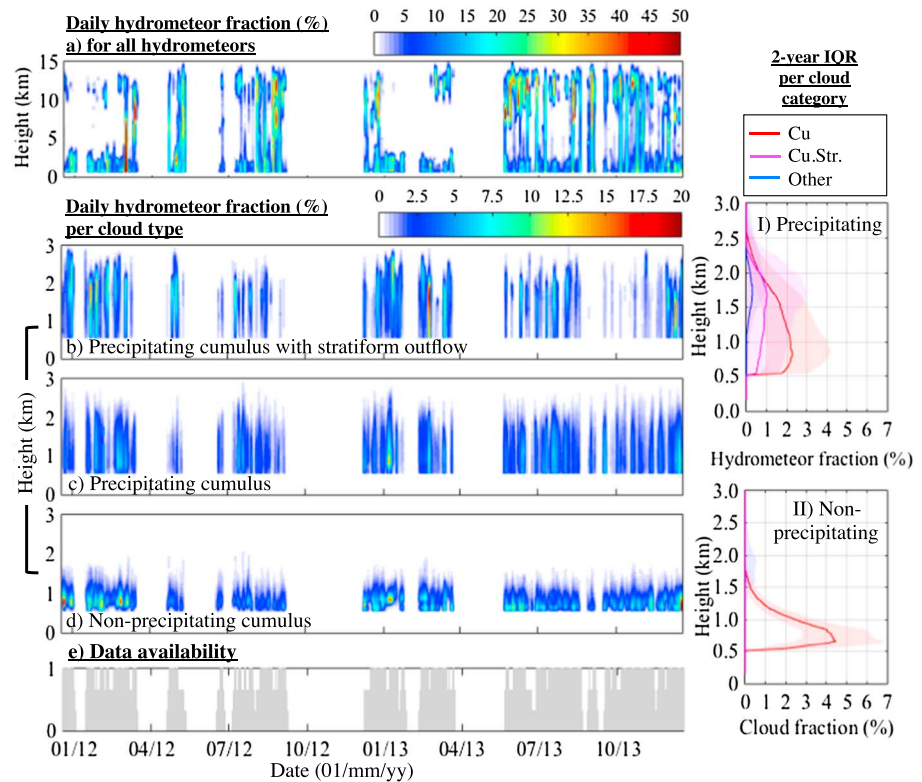
Figure 4. Two-year time series of (a) daily hydrometeor fraction in the troposphere for all hydrometeors (clouds and precipitation) and daily hydrometeor fraction in the boundary layer per cloud type (b) precipitating cumulus with stratiform outflow, (c) precipitating cumulus, (d) nonprecipitating cumulus, also included (e) binary radar data availability; all following the 3 day smoothing. To the right is the interquartile range (IQR) of hydrometeor fraction (from the 2 year time series) per boundary layer cloud category: (I) Precipitating clouds and (II) Nonprecipitating clouds; both using the unsmoothed data set. In the nonprecipitating clouds (Figure 4II), cloud fraction instead of hydrometeor fraction is indicated, since in the absence of precipitation the only hydrometeors present are clouds.

a minimum in January–March. The highest cloud tops reach 14–15 km, and their extent exhibit small seasonal variability.

The contribution of the three main MBL cloud types to the total observed MBL hydrometeor fraction (Figure 4a) is shown in Figures 4b–4d. The interquartile range (IQR) of the observed daily hydrometeor fraction vertical profile from each cloud type is shown in Figures 4I and 4II (These vertical profiles are computed using physical height and as such do not account for day-to-day cloud base height variations on the order of ±150 m [*Nuijens et al.*, 2014] which may slightly smear the cloud fraction peaks vertically). Figure 4I shows that precipitating cumuli have a hydrometeor fraction that peaks at 2.3% at 809 m, whereas when precipitating cumuli are accompanied with stratiform outflow, they have peak hydrometeors fraction of 1% at 1679 m (see also Figure 2b). Finally, other clouds with elevated bases contribute 0.3% of the cloud fraction. The two precipitating cumulus classes seem to occur concurrently throughout the year (Figures 4b and 4c), although there is a noticeable absence of precipitating boundary layer clouds in September–November 2013 (no data available in 2012) and higher occurrence of stratiform layers in the January–March of both years. Furthermore, the presence of precipitating clouds is intermittent with periods of 3–5 days of precipitating conditions followed by dry conditions.

The nonprecipitating clouds have a cloud fraction that peaks at a much larger value of 4.5% at 660 m (Figure 4II). On a day-to-day basis, this peak value varies between about 3% and 6% (interquartile range), which means that every day exhibits at least some cloudiness at this level. Seasonality in cloudiness at this level is overall weak [see also *Nuijens et al.*, 2014] and is opposite to that of the deeper cumuli and cirrus clouds, which dominate during summer (Figures 4d and 4a).

### 3.2. The Internal Structure of Individual Cumulus Clouds

In the absence of precipitation, reflectivity (Z) is related to liquid water content and Doppler velocity (V) to vertical velocity. In the presence of precipitation, these relationships are more complex; nevertheless, reflectivity and velocity can be used to make educated guesses on precipitation strength. Here we will have a closer look at the internal structure of individual cumulus clouds by means of these two quantities (Z and V).

The maximum vertical and temporal extent of each individual cumulus are used to create a normalized coordinate system ($-1{:}1$, $-1{:}1$) where -1 and 1 correspond to the first and last cloud detection in time and height, respectively. Note that in the case of cumulus with stratiform outflow, only the cumulus segment is considered (e.g., Figure 1c, clear box). As such (0,0) corresponds to the center of each cumulus. Using a spacing of 0.05, this framework creates a 21×21 grid onto which each cloud is interpolated. This analysis has the caveat that clouds may not necessarily pass the radar along their central longest axes. The availability of a large number of sampled clouds (hundreds and more depending on the cloud type; Table 1) should, however, minimize possible biases.

Using this normalization grid, all members of a particular class of MBL cloud can be overlapped together to produce, for each grid point individually, percentiles of radar reflectivity and mean Doppler velocity (Figure 5). Radar reflectivity is shown in colors, whereas the Doppler velocity is shown in contour lines. The plotted percentiles thus represent the median behavior of all clouds at a given grid location but is similar to the behavior of any individual cloud (not shown). Statistics of the actual dimensions of individual clouds are provided in Table 1.

The radar reflectivity percentiles of the nonprecipitating cumulus clouds are characterized by an elevated reflectivity maximum (IQR (-40 to 28) dBZ) located near the cloud top (Figure 5, top row, color map). At each quartile, an average vertical increase of 15 dB is observed from the cloud base to the center of the reflectivity core. This radar reflectivity structure is consistent with shallow cumulus clouds where condensation is the main mechanism for hydrometeor growth. At the same time, the lateral cloud boundaries are characterized by lower radar reflectivities, in fact, a 10 dB horizontal increase in the radar reflectivity is observed from the lateral boundaries to the core. This is consistent with the presence of lateral environmental mixing that reduces the droplet sizes through evaporation and subsequently reduces their radar reflectivity. As we progress toward higher quartiles (Figure 5, top row from left to right), the elevated reflectivity core expands vertically and horizontally. Overall, the normalized maps of radar reflectivity of the nonprecipitating clouds are consistent with the radar view of clouds that contain no or very little large droplets. In addition, the normalized maps of mean Doppler velocity of the nonprecipitating cumulus are shown in Figure 5 (top row, contours). Once again, the velocity fields illustrate well-defined elevated updraft cores with IQR (0.65 0.00) m s^{-1}. The elevated updraft core is observed in all three percentiles. However, a noticeable decrease in the updraft magnitude is observed across quartiles. The 25th and 50th percentiles show strictly upward vertical motion, while the 75th percentile shows a band of downward motion concentrated on the lateral boundaries. A plausible explanation for this transition is to view the three percentiles as three different life stages of the nonprecipitating shallow cumulus clouds. Initially, the cloud is very active and buoyant (25th percentile) and gradually due to environmental stability and mixing loses momentum (50th percentile) and eventually becomes dynamical inactive with signs of evaporating downdrafts around its lateral boundaries.

The interpretation of the normalized maps of radar reflectivity and mean Doppler velocity for the two categories of precipitating clouds (without and with stratiform outflow) is more challenging due to the presence of large particles that dominate both to the observed radar reflectivity and mean Doppler velocity. The normalized maps of radar reflectivity have similar structure in both precipitating cumulus categories (Figure 5, middle and bottom rows, color map). The differences between them are mostly evident in the magnitude of the overall reflectivity. Roughly, from the 25th to 75th percentiles, clouds with outflow layers have 5, 7, and 11 dB higher reflectivities. The precipitating clouds initially (at the 25th percentile) appear similar to the 75th percentile of the nonprecipitating clouds because they contain an elevated reflectivity core, yet their vertical gradient is 10 dB weaker. We attribute this difference to the presence of weak precipitation. Furthermore, as we progress toward higher percentiles, the elevated reflectivity core and associated vertical gradient eventually vanish (the vertical gradient from the base to
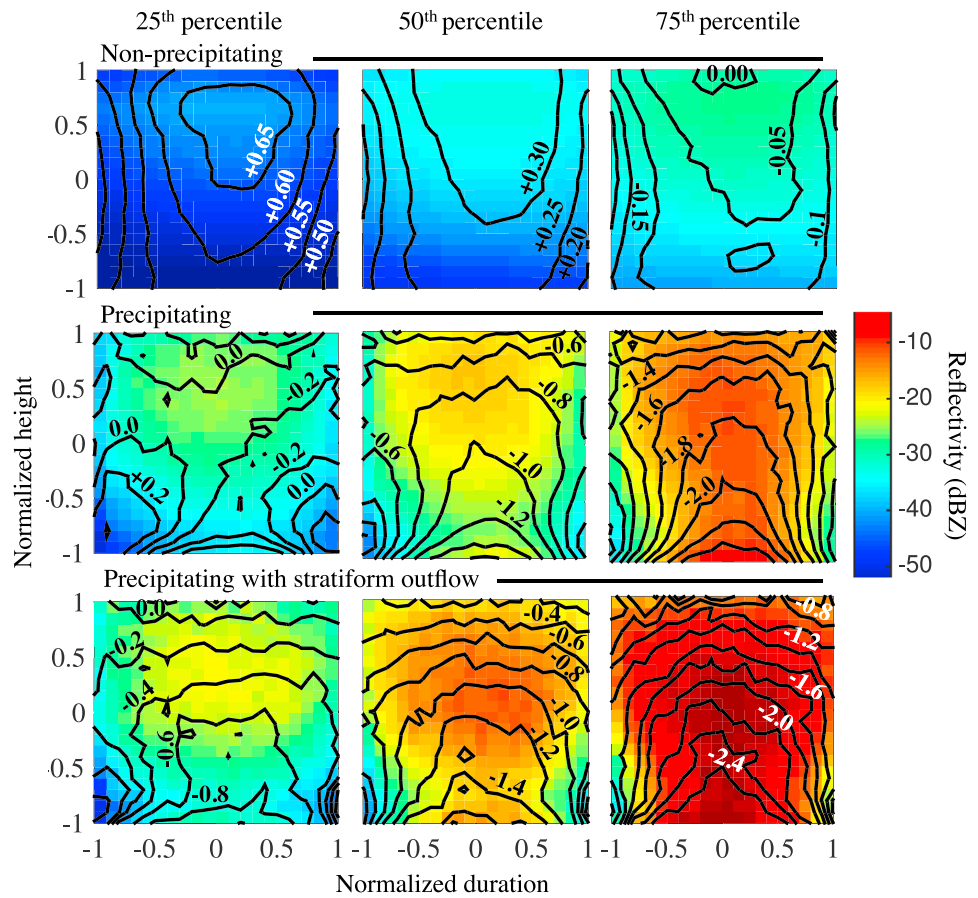
Figure 5. Normalized cloud reflectivity color map and Doppler velocity contours composites. (left column) 25th percentile, (middle column) 50th percentile, (right column) 75th percentile. (top row) Nonprecipitating cumulus, (middle row) precipitating cumulus, and (bottom row) cumulus segment of the precipitating cumulus with stratiform outflow.

the core changes from +6 dB at the 50th percentile to 0 dB at the 75th percentile). This radar signature is consistent with the presence of large drop that grows via accretion as they fall toward the cloud base. The descending raindrops increase the radar reflectivity of the lower part of the clouds and thus cause the reduction in the vertical gradient of the radar reflectivity. In terms of the Doppler velocity, both precipitating cloud categories contain only downward mean Doppler velocities. The observed increase in the downward mean Doppler velocity from the cloud top to the cloud base is also consistent with the accretional growth of the raindrops. Clouds with outflow detrain layers show downward mean Doppler velocities that are 0.20 m s^{-1} stronger at the cloud top, this combined with the observed higher reflectivity suggests that they contain more intense rain.

4. The Mass Flux Structure of Nonprecipitating Cumuli

The KATRIN mean Doppler velocity can be used to retrieve the vertical air motion and estimate the magnitude of updrafts and downdrafts in cumuli and their fractional coverage relative to the entire sky (clear and cloudy). Combined, these provide the in-cloud mass flux. In this section, we identify the updraft and downdraft structures and quantify their respective contribution to the mass transport. It is important to note that the mass flux analysis is limited to nonprecipitating cumuli because it requires that the observed radar Doppler velocities can be considered as a proxy for air motion.

Vertical velocity and mass flux statistics will be derived for each 3 h periods in which only nonprecipitating clouds occur. The use of a 3 h averaging period should provide a large enough data sample to average out the life cycles of individual clouds and produce robust statistics. This averaging time can be converted to a
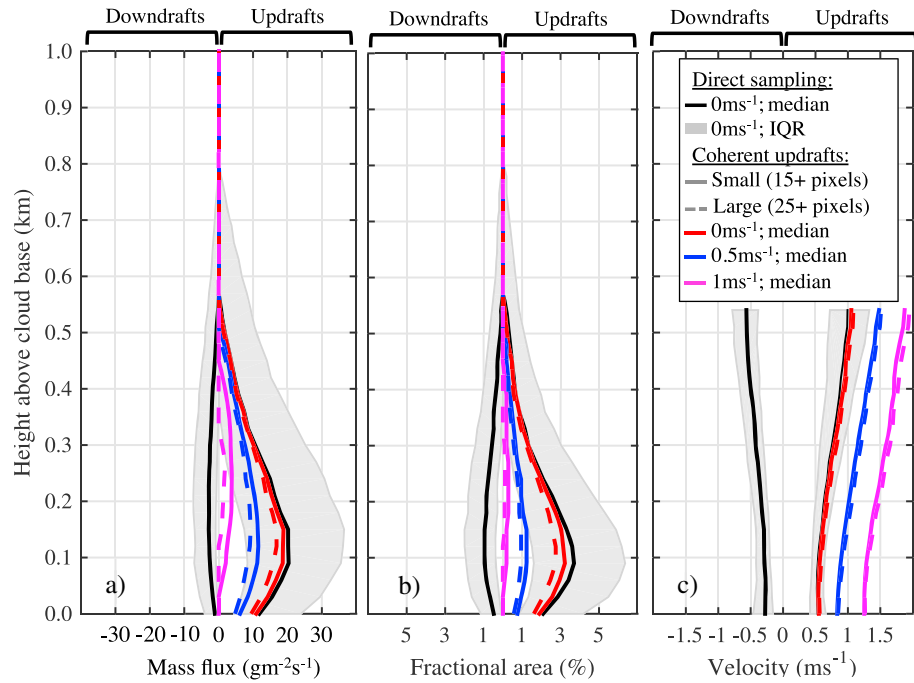
Figure 6. Profiles of (a) mass flux, (b) fractional area, and (c) vertical velocity above cloud base for nonprecipitating cumulus using 3 h averaging periods. Results from direct sampling (considering all updrafts and downdrafts) are in black (solid line: median, envelope: 25th–75th percentiles). Colored solid lines show results from sampling small coherent updraft (15 pixels or more), the different colors represent the various vertical velocity thresholds used to capture stronger updrafts (solid lines: median; $0\,\mathrm{m\,s^{-1}}$ (red), $0.5\,\mathrm{m\,s^{-1}}$ (blue), and $1\,\mathrm{m\,s^{-1}}$ (pink)). Similarly, colored dashed lines represent results from sampling large coherent updrafts (25 pixels or more).

corresponding length scale using an average wind speed of $8\,\mathrm{m\,s^{-1}}$, which gives 86.4 km, comparable to the grid size of any modern general circulation model.

A total of 1003 three-hour periods (i.e., 3009 h; Table 1) satisfied this criterion, which is the largest available data set to date for oceanic shallow cumuli and should be sufficient to derive robust statistics. We estimate, above the 3 h-averaged cloud base height, the mean updraft velocity at each height (w_{up}; estimated by all points with $w > 0\,\mathrm{m\,s^{-1}}$), the updraft fractional coverage (a_{up}; estimated as the number of points in 3 h with $w > 0\,\mathrm{m\,s^{-1}}$ divided by the total number of observations cloudy or not in 3 h), and the updraft mass flux.

$$M_{up} = a_{up} w_{up} \tag{3}$$

The corresponding profiles for downdrafts ($w < 0\,\mathrm{m\,s^{-1}}$) are also estimated. Note that traditionally the mass flux is calculated using the draft velocity departure from the mean atmospheric velocity. However, given that the radar only samples the cloudy part of the atmosphere, we have to rely on the usual assumption that mean atmospheric vertical air motion at every level is $0\,\mathrm{m\,s^{-1}}$ [Ghate et al., 2011; Kollias and Albrecht, 2010]. In the trades, the subsidence velocity is on the order of $0.005\,\mathrm{m\,s^{-1}}$ [Nuijens et al., 2014] which is negligible relative to cloudy draft velocities on the order of $0.5\,\mathrm{m\,s^{-1}}$. Finally, also for simplicity, air density is reasonably assumed constant at $1\,\mathrm{kg\,m^{-3}}$. The median (black line) and IQR (shaded region) of the data are presented in Figure 6, as a function of height above cloud base. One panel is presented per parameter (M, Figure 6a; a, Figure 6b; and w, Figure 6c). In each panel, the right portion (positive x axis) is dedicated to the updrafts, while the left portion (negative x axis) is dedicated to the downdrafts. For references, Table 2 contains tabulated values at key heights.

Furthermore, the contribution of coherent (in time-height) updraft structures is investigated. To account for tilted updrafts as described in literature [Ghate et al., 2011], in time-height, each cluster of velocity echoes above the velocity threshold ($w > 0\,\mathrm{m\,s^{-1}}$) larger than 15/25 pixels is defined as a coherent structure. Two size thresholds (15+ and 25+) are used to illustrate the lack of dependency of our results on the size threshold used to define a coherent eddy. Two additional velocity thresholds (0.5 and $1.0\,\mathrm{m\,s^{-1}}$) are

Table 2. Tabulated Percentile Values of Mass Flux, Area, and Velocity at Key Height Levels From the Profiles Illustrated in Figure 6

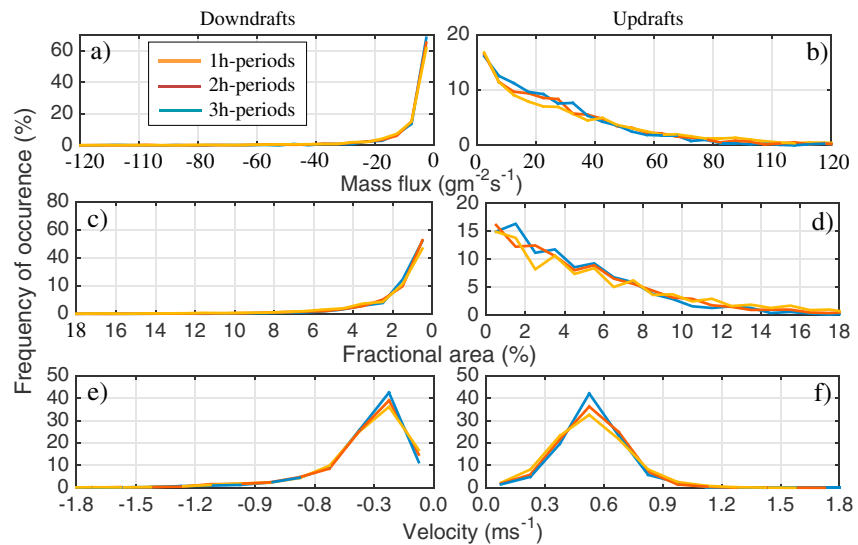|	Mass Flux (gm^{-2} s^{-1})			Fractional Area (%)			Velocity (m s^{-1})		
	Up. 50th 25th/75th	Coherent Up. 0 m s^{-1} 15 + pixels 50th	Down. (−) 50th 25th/75th	Up. 50th 25th/75th	Coherent Up. 0 m s^{-1} 15 + pixels 50th	Down. 50th 25th/75th	Up. 50th 25th/75th	Coherent Up. 0 m s^{-1} 15 + pixels 50th	Down. (−) 50th 25th/75th
At the updraft mass flux peak	20 8/36	19	3 0/7	3.7 1.6/6.4	3.2	1.0 0.4/1.9	0.53 0.45/0.64	0.564	0.29 0.20/0.42
At cloud base	12 5/24	11	1 0/4	2.1 0.9/4.2	1.9	0.5 0.1/1.1	0.53 0.42/0.66	0.55	0.28 0.16/0.46
Maximum value Height (km)	20 0.09	19 0.09–0.15	3 0.15–0.24	3.7 0.09	3.2 0.09	1.0 0.09–0.15	0.10 0.57	1.05 0.57	0.57 0.57
Minimum value Height (km)	0 0.57	0 0.57	0 0.57	0.0 0.57	0.0 0.57	0.0 0.57	0.52 0.03	0.54 0.03	0.27 0.03

included to derive the statistics of more intense coherent updrafts. For the coherent updraft sampling, only the median (colored lines) of the 2 year sample is presented in Figure 6. The various velocity thresholds take different colors (0 m s^{-1}, red; 0.5 m s^{-1}, blue; and 1 m s^{-1}, pink). The various size thresholds are indicated using different line types (15+ pixels, solid; 25+ pixels, dashed). For references, Table 2 contains tabulated values of the coherent updrafts, 15 pixels, 0 m s^{-1}, at key heights.

Figure 6c shows that the velocity of both updrafts and downdrafts (black lines, respectively, on the positive and negative x axis) is invariant with height in the first 150 m above the cloud base. Above this level, the draft magnitudes increase rapidly to reach their maximum value just below cloud top. Overall, at all levels, the updraft magnitude is higher than that of downdrafts, and the width of the distributions increases with height. The shape of the coherent updraft velocity profiles (colored lines) is similar, but their magnitude is greater, simply reflecting the larger velocity threshold used.

The shape of the direct updraft fractional area profile (Figure 6b, black line on the positive x axis) follows the cloud fraction profile of nonprecipitating cumuli (shown in Figure 4II), in which most of the clouds are concentrated within a 0.3 km thick layer above cloud base. The updraft area profile peaks 0.09 km above cloud base and decreases rapidly to zero 0.57 km above the cloud base height. The area occupied by the coherent structures peaks at a greater height as the velocity threshold chosen increases in magnitude (depicted by the vertical translation of the peak from the red curve to the blue curve to the pink curve). The 0.0, 0.5, and 1.0 m s^{-1} coherent updraft profiles peak at heights 0.09, 0.09–0.15, and 0.18–0.27 km with values 3.2%, 1.2%, and 0.3%, respectively. Notice how the coherent updraft structures do not span the entire depth of the cloud layer. The median fractional coverage of the 1.0 m s^{-1} updraft coherent structures is zero near the cloud base and the cloud top (pink line). This indicates that 1.0 m s^{-1} updraft coherent structures are not present near the cloud vertical boundaries. Incidentally, the direct downdraft area profile does not have very pronounced peak values (black line on the negative x axis). The direct updraft area is systematically larger and more variable than that of the direct downdraft area (IQR ~5% versus ~2%). This supports the results of the 2-D analysis presented in the previous section (Figure 5b, contours), namely, inside nonprecipitating cumuli, the downdraft shells are narrow whereas the central core of clouds with stronger updrafts is wider.

Finally, we find that the shape of the direct mass flux profiles (Figure 6a, black lines), which is calculated as the product of the mean area and velocity profiles, is mainly influence by the area profile (Figure 6b, black lines). The direct updraft mass flux peaks at 0.09 km above cloud base at a value of 20 gm^{-2} s^{-1}, which coincides with coherent updraft (15+ pixels, $w > 0$ m s^{-1}) transport of 19 gm^{-2} s^{-1} or 95% of the direct mass flux. The mass flux from stronger coherent updrafts peaks at different heights, 0.5 m s^{-1} at 0.09 km with 12 gm^{-2} s^{-1} and 1 m s^{-1} at 0.24 km with 4 gm^{-2} s^{-1}.

The full histograms of the parameters (M, a, w) at the height of the mass flux maximum (0.09 km) are extracted from the black profiles depicted in Figure 6. Keep in mind that these results are produced using 3 h statistics over a 2 year data set (Figure 7, blue lines). In order to investigate the stability of the mass flux

Figure 7. Distribution at the mass flux peak (0.09 km above cloud base) of downdraft (a) mass flux, (c) fractional area, and (e) velocity and updraft (b) mass flux, (d) fractional area, and (f) velocity for nonprecipitating cumulus periods using three different averaging periods (1 h (yellow), 2 h (red), and 3 h (blue)).

on various scales, we also reproduce these statistics using 2 h and 1 h averaging periods (Figure 7; red and yellow lines respectively). The three distributions are very similar; the only discrepancy is a slight increase in the variance and subsequent elongation of the tail of the distribution with decreasing averaging period.

We find that the updraft mass flux distribution is broad and mostly related to the broad distribution of fractional area (Figures 7b and 7d). The downdraft mass flux distribution has smaller spread and contains a preferred mode at $0–5\,\mathrm{g\,m^{-2}\,s^{-1}}$ (Figure 7a). Overall, the updrafts are wider than downdrafts (Figures 7c and 7d). The updraft velocity distribution is nearly symmetrical about $0.5\,\mathrm{m\,s^{-1}}$, while the downdraft velocity distribution peaks at $-0.2\,\mathrm{m\,s^{-1}}$ and has a tail elongating to about $-1.3\,\mathrm{m\,s^{-1}}$. Hence, narrow downdrafts do not seem more vigorous than updrafts (Figures 7e and 7f).

## 5. Relationships to Environmental Thermodynamic Profiles

Vertical and lateral mixing of cloudy and environmental air is known to impact the mass flux profile in cumulus clouds; hence, it is reasonable to hypothesize that variations in boundary layer temperature and humidity could explain some of the variability in cloudiness and mass flux that we find. As stated in section 1, we make such a first exploration by making use of 3 months of nighttime simultaneous radar and Raman lidar measurements.

First, to investigate if environment thermodynamics play a role in the height shift of the location of the maximum cloud fraction, profiles of relative humidity and temperature are estimated within a 1 h window of each precipitating cloud. Figure 8 blue profiles represent the mean for cumuli with enhanced upper level cloudiness, and red profiles represent the mean for cumuli with enhanced low-level cloudiness. One can see that the temperature profiles are virtually identical, and the temperature inversion is not pronounced. Adversely, the relative humidity inversion is more distinct, and this is where differences between the two cloud types arise. The presence of stratiform layers in the 1.5–2 km region coincides with the presence of increased environmental moisture. Note that no attempt will be undertaken here to disentangle the role of clouds and precipitation on relative humidity.

Second, mass flux has an inherent relationship to both thermodynamics and cloud layer depth in parameterization schemes. In order to isolate the effect of environmental conditions *de Rooy and Siebesma* [2008] proposed to study nondimensional mass flux as a function of nondimensional height.

$$\hat{M} = M/M_b \tag{4}$$

$$\hat{Z} = (Z - Z_b)/(Z_t - Z_b) \tag{5}$$
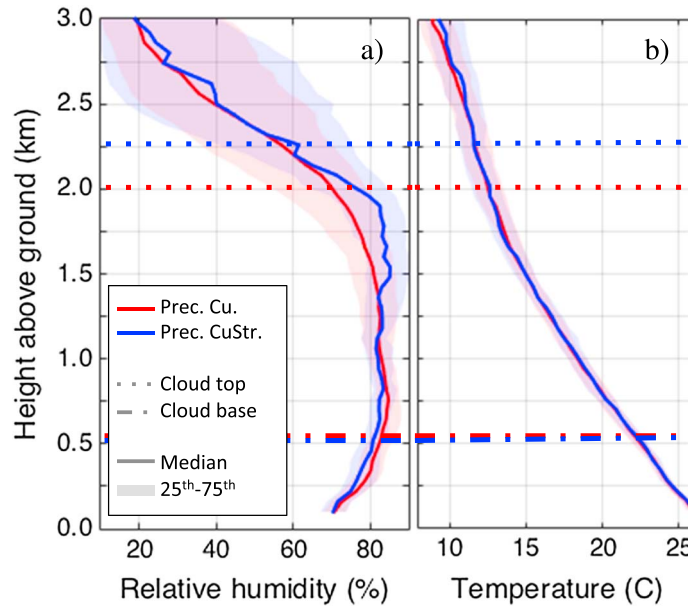
Figure 8. Mean thermodynamic profiles averaged within an hour of precipitating cumulus (red) or precipitating cumulus with increased elevated cloudiness (blue) of (a) relative humidity and (b) temperature. Solid lines are median values and shaded regions represent the 25th and 75th percentiles. Also included are horizontal dotted lines and dashed lines, respectively, most occurring cloud top and base.

where the subscript b refers to the height with maximum updraft mass flux and t refers to the first height with zero mass flux (i.e., cloud top). Additionally, *de Rooy and Siebesma* [2008] parameterized the mass flux in two parts, below and above the normalized center ($\hat{Z} = 0.5$). To emulate this technique with simplicity, we used a linear relationship from the maximum updraft mass flux ($\hat{Z} = 0$) to the center of the profile ($\hat{Z} = 0.5$; lower slope) and from the center of the profile to the top ($\hat{Z} = 1$; upper slope). As a result, the updraft mass flux magnitude in the center of each profile dictates both slopes. We find that this linear approximation is accurate ($R^2 > 80\%$) in 47.8% of the cases for the upper slope and 58.8% of the cases for the lower slope. However, even if often imprecise, this approximation conserves the inherent trends of the data (i.e., concave profiles have the largest absolute value slopes or fastest mass flux reduction with height).

Recall that our analysis was previously limited to periods containing no precipitating clouds because they reduce the horizontal area coverage of updrafts. However, in this section, because the profiles are nondimensional (the maximum mass flux is always 1), we can simply mask precipitating clouds when present, without discarding the complete 3 h period. Hence, all 2390 3 h periods (i.e., 7,170 h; Table 1) of radar observations are used to produce a joint probability function of the normalized updraft mass flux against normalized height (Figure 9b). The normalized updraft mass flux profile slopes are computed as the change in normalized updraft mass flux per 0.1 unit normalized height for $0 < \hat{Z} < 0.5$ (d$\hat{M}$/0.1d$\hat{Z}$). The distribution of the normalized updraft mass flux slope in the lower half of the cloud layer is presented in Figure 9a. Note that the lower and upper slope distributions would be symmetrical because both are linear trends of the normalized updraft mass flux rooted in the center of the cloud layer. In Figures 9a and 9b, arrows are used to indicate the cases where the lower slope is larger in magnitude than the upper slope, i.e., where the mass flux reduction with height is larger in the lower part of the cloud layer rather than in the upper part.

The probability density function, its median, and IQR (black circle and whiskers) give us a comprehensive visual of the normalized mass flux profiles of the entire population and can be compared to work presented in previous studies (Figure 9b; also see section 6). The normalized updraft mass flux at the center of the cloud layers, critical to determine its slope, varies around a median value of 0.38 (IQR (0.24 0.53)). The majority (71.8%) of the observed nondimensional mass flux profiles are concave (d$\hat{M}$/0.1d$\hat{Z} < -0.1$ in the lower part of the cloud layer), and as a result, the lower slope distribution peaks at -0.13 d$\hat{M}$/0.1d$\hat{Z}$ (Figure 9a).
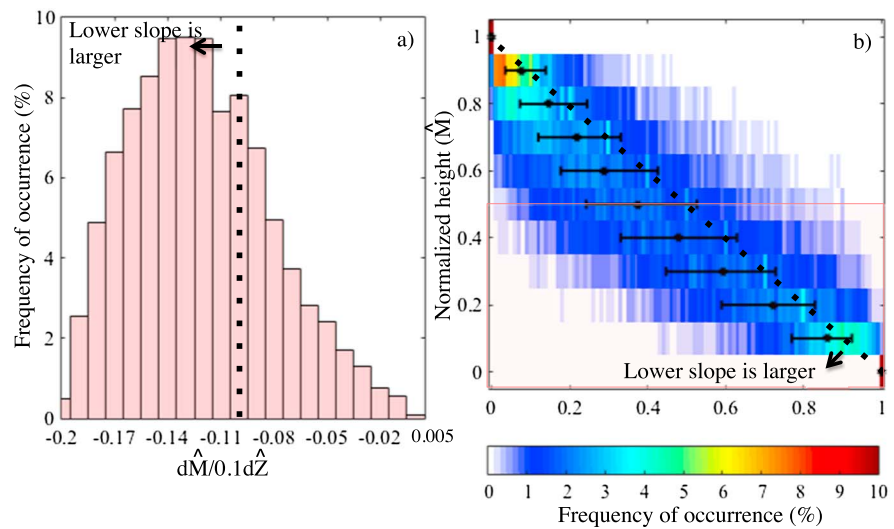
Figure 9. (a) Distribution of the normalized updraft mass flux profile slope in the lower half of the cloud layer. (b) Joint probability function of normalized updraft mass flux per normalized height. Included are the 0.1 slope (dotted line), the normalized updraft mass flux median (circle), and the interquartile range (whiskers) at each normalized height.

This indicates that most clouds lose their mass more quickly in the lower part of the cloud layer. Alternatively, 8.7% of the observed cases are linear (-0.1 d$\hat{M}$/0.1d$\hat{Z}$ slopes), and the remaining 19.5% are convex.

To investigate the relationship between the shape of the updraft mass flux profiles and the environmental thermodynamic profiles, the lower slope distribution is separated in three sections: -0.03 to -0.09, -0.09 to -0.14, and -0.14 to -0.19 d$\hat{M}$/0.1d$\hat{Z}$. The corresponding thermodynamic profiles retrieved by the Raman lidar are averaged with respect to height from the ground to produce Figure 10. Figure 10a shows that there is a progressive increase in mean relative humidity, at heights above 1 km closer to the cloud tops, with decreasing mass flux slope. Differences in temperature, however, are small. Results that are more robust could potentially be achieved once the complete Raman lidar data set is released.

6. Main Findings and Relevance to Previous Studies

In this study, we take advantage of a long record (403 days across 2 years) of zenith pointing cloud radar observations at the Barbados Cloud Observatory (BCO) to describe the oceanic shallow cumulus cloud field. The description spans various physical and temporal scales (ranging from individual clouds to cloud ensembles and from daily to hourly statistics) and encompasses radar and "model-like" parameters (e.g., reflectivity, velocity, cloud fraction, and mass flux). Furthermore, we investigate the relationship between some of the cumulus cloud field variability and environmental thermodynamics as observed by the Raman lidar (3 month data set during nighttime). Throughout the analysis, we discuss mainly two marine boundary layer cloud types: Cumulus and cumulus with attached stratiform segments and identify if individual clouds contain precipitation size droplets, which impacts the radar observables.

At the BCO, nonprecipitating cumulus contribute the most to the observed hydrometeor fraction (peak 4.5% at 710 m) relative to precipitating cumulus without (peak 2.3% at 809 m) and with attached stratiform segments (peak 1% at 1679 m). All MBL cloud types experience similar temporal variability (IQR ~3%). Our analysis suggests that in December–April (during periods of large-scale subsidence as reported in B. Stevens et al., in preparation, 2014) deep cloud systems are suppressed at the expense of more and deeper cumulus clouds and higher occurrence of stratiform outflows. It is possible that the large-scale subsidence helps maintain the compensating clear air downdrafts around the vigorous nonprecipitating cumulus. Moreover, this subsidence may help sustain the observed moisture inversion occurring with the detrained stratiform layers up top deep precipitating cumulus. On a different note, a review of relevant literature indicates the lack of consensus on the nonprecipitating subtropical cumulus cloud fraction
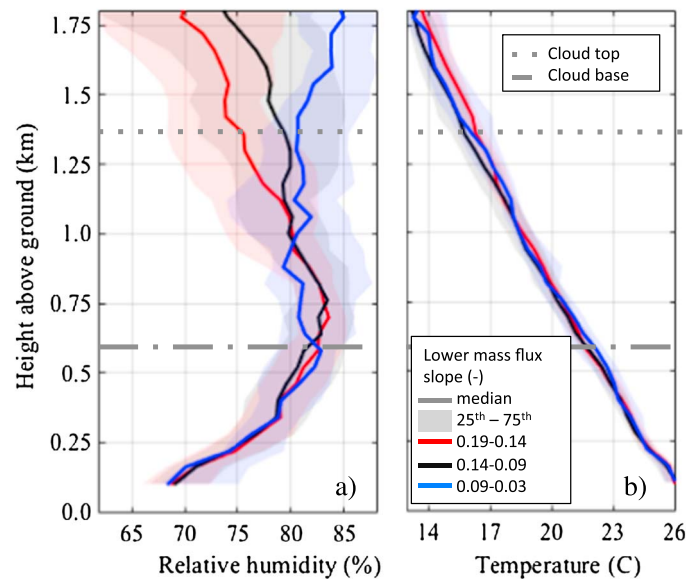
Figure 10. Thermodynamic profiles for different intervals of normalized updraft mass flux profile slope in the lower half of the cloud layer (a) relative humidity and (b) temperature. Solid lines are median values and shaded regions represent the 25th and 75th percentiles. Also included are horizontal dotted lines and dashed lines, respectively, approximate cloud top and base of the nonprecipitating cumuli.

magnitude, and significant variability has been reported (e.g., The Azores 5.7%, [*Ghate et al.,* 2011]; Nauru 15%, [*Kollias and Albrecht,* 2010]; and Barbados 10%, [*Nuijens et al.,* 2014]). Very likely, the observed discrepancies are attributed to the instruments and methodologies used in the various studies. The BCO radar is one of the most sensitivity ground-based radars and thus is expected to detect most if not all radiatively significant shallow cumuli. Yet it is plausible that our conservative definition of nonprecipitating cloud (section 2.3) is partially responsible for the modest reported cloud fraction.

The normalized cloud composites of shallow nonprecipitating cumuli indicate the presence of an elevated maximum radar reflectivity core surrounded by lower reflectivities. This is consistent with the radar view of a cloud where condensation and evaporation (enhanced on the lateral boundaries) are the primary mechanisms that control the particle size distribution. The reported 15 dB reflectivity increase from cloud base to cloud core (reflectivity maxima) at the center of cloud composites is consistent with previous studies [*Ghate et al.,* 2011]. The observed positive median velocity ($0.25 \, \mathrm{m \, s^{-1}}$) across the cloud is comparable to those observed at the Azores (mean velocity around $0.33 \, \mathrm{m \, s^{-1}}$) [*Ghate et al.,* 2011] and Nauru (rising motions across 80% of their height with mean velocity between 0.10 and $0.35 \, \mathrm{m \, s^{-1}}$) [*Kollias and Albrecht*, 2010]. Also, the existence of subsiding shells (downdraft velocities near the lateral cloud boundaries) was investigated in a modeling study by *Heus and Jonker* [2008] and further observed by aircraft-based studies [*Heus et al.,* 2009]. As for the features of updrafts and downdrafts: In their BOMEX modeling study, *Siebesma and Cuijpers* [1995] succeeded at reproducing the observed increase in updraft velocity with height but generated velocity gradients steeper than those found here. Similarly, observations by *Kollias and Albrecht* [2010] indicate higher downdraft magnitude at cloud base and top (almost a factor of 2 stronger).

The normalized cloud composites of precipitating cumulus are consistent with the expected radar view of clouds where precipitation processes are active and particles are larger. The radar reflectivities are higher, and the vertical gradient of the radar reflectivity is reduced or even reversed. This is consistent with the presence of large raindrops in the lower part of the cloud that grow via accretion. The mean Doppler velocity is downward due to contribution of the large drops and increases towards the cloud base, a signature that is also consistent with particle growth via accretion. Our results show that precipitating cumulus clouds that develop an elevated cloud layer are deeper and have higher reflectivity and velocity magnitudes and gradients, all of which are consistent with more developed mature clouds.

Due to the influence of raindrops on the observed mean Doppler velocity, only the dynamical structure of nonprecipitating cumuli is investigated. Overall, the Barbados nonprecipitating cumuli are very organized and active. In-cloud velocities consist of 78% of updrafts in the lower part of the cloud layer, similar to that reported by *Kollias and Albrecht* [2010] (70%) but larger than modeled by *Siebesma and Cuijpers* [1995] (51%). Moreover, throughout most of the cloud layer, 86% of them are coherent structures, which is significantly higher than previously found by *Ghate et al.* [2011] (~62%) using a slightly different definition. This finding is in agreement with the use of Large Eddy Simulations (LES) that attempt to explicitly represent mass transport in shallow cumulus by resolving only the main eddies. Our 15/25 radar pixels or larger coherent structures correspond to about 3×5 (time $\times$ height) radar pixels or $240 \, m \times 150 \, m$ (assuming an $8 \, m \, s^{-1}$ horizontal wind). It is also determined that the location of the updraft area peak rather than the velocity maxima determines the location of the updraft mass flux peak which magnitude we report is median 20 IQR (8 36) $gm^{-2} s^1$. This value is directly comparable to that measured by *Ghate et al.* [2011] at the Azores. It is however lower than the $90 \, gm^{-2} s^{-1}$ at Nauru reported by *Kollias and Albrecht* [2010]. It should be noted that cloud fraction is much larger in Nauru (~15%), and scaling the updraft mass flux with cloud fraction reconciles both results. The mass flux that we calculate is similar to that derived from LES in *Siebesma and Cuijpers* [1995]; however, this is a combination of smaller updraft fractions in LES as well as larger updraft velocities. This shows the importance to compare all mass flux contributors to validate parameterizations. Moreover, our analysis indicates that the in-cloud downdrafts have relatively small mass flux and very weak vertical and temporal variance. The downdraft mass flux does not compensate for the in-cloud updraft mass flux as was modeled by *Siebesma and Cuijpers* [1995]. This suggests that most of the compensating downdraft motions occur in clear air and that in-cloud downdraft mass flux is rather negligible.

Finally, observational evidence was presented to support the presence of an inverse relationship between the environmental humidity and the rate of vertical decrease of the updraft mass flux in nonprecipitating cumuli. The updraft mass flux profiles normalized to isolate the effect of environmental thermodynamic from cloud layer depth (Figure 9b) may be compared to that of *de Rooy and Siebesma* [2008, Figure 9]. Notice that both studies contain more concave than convex mass flux profiles and show a similar spread of values. Moreover, they share a similar midcloud layer normalized mass flux (0.3 versus 0.38). This concave behavior indicates that clouds lose their mass more quickly in their lower half. *Zhang and Klein* [2013] performed parallel work when they explored the role of relative humidity on cloud vertical extent. They found that continental fair-weather cumuli are thicker when boundary layer relative humidity is larger, supporting the idea that clouds present in a moister environment evaporate (i.e., reduce their mass flux) more slowly upon mixing with the environment than the clouds present in dryer conditions. These sets of observational evidence encourage the use of a distinct relationship between mass flux and relative humidity in parameterizations.

References

Bauer-Pfundstein, M. R. (2007), Target separation and classification using cloud radar Doppler-spectra.

Bechtold, P., et al. (2008), Advances in simulating atmospheric variability with the ECMWF model: From synoptic to decadal time-scales, *Q. J. R. Meteorol. Soc.*, *134*(634), 1337–1351, doi:10.1002/qj.289.

Beniston, M. G., and G. Sommeria (1981), Use of a detailed planetary boundary layer model for parameterization purposes, *J. Atmos. Sci.*, *38*, 780–797, doi:10.1175/1520-0469(1981)038%3C0780:UOADPB%3E2.0.CO;2.

Chandra, A. S., P. Kollias, and B. A. Albrecht (2013), Multiyear summertime observations of daytime fair-weather cumuli at the ARM Southern Great Plains facility, *J. Clim.*, *26*(24), 10,031–10,050, doi:10.1175/JCLI-D-12-00223.1.

de Rooy, W. C., and A. P. Siebesma (2008), A simple parameterization for detrainment in shallow cumulus, *Mon. Weather Rev.*, *136*(2), 560–576, doi:10.1175/2007MWR2201.1.

Derbyshire, S. H., I. Beau, P. Bechtold, J.-Y. Grandpeix, J.-M. Piriou, J.-L. Redelsperger, and P. M. M. Soares (2004), Sensitivity of moist convection to environmental humidity, *Q. J. R. Meteorol. Soc.*, *130*(604), doi:10.1256/qj.03.130.

Eastman, R., S. G. Warren, and C. J. Hahn (2011), Variations in cloud cover and cloud types over the ocean from surface observations, 1954–2008, *J. Clim.*, *24*(22), 5914–5934.

Frisch, A. S., C. W. Fairall, and J. B. Snider (1995), Measurement of stratus cloud and drizzle parameters in ASTEX with a Kα-band Doppler radar and a microwave radiometer, *J. Atmos. Sci.*, *52*(16), 2788–2799, doi:10.1175/1520-0469(1995)052<2788:MOSCAD>2.0.CO;2.

Ghate, V. P., M. A. Miller, and L. DiPretore (2011), Vertical velocity structure of marine boundary layer trade wind cumulus clouds, *J. Geophys. Res.*, *116*, D16206, doi:10.1029/2010JD015344.

Heus, T., and H. J. J. Jonker (2008), Subsiding shells around shallow cumulus clouds, *J. Atmos. Sci.*, *65*(3), 1003–1018, doi:10.1175/2007JAS2322.1.

Heus, T., C. F. J. Pols, H. J. J. Jonker, H. E. A. Van den Akker, and D. H. Lenschow (2009), Observational validation of the compensating mass flux through the shell around cumulus clouds, *Q. J. R. Meteorol. Soc.*, *135*(638), doi:10.1002/qj.358.

Hildebrand, P. H., and R. S. Sekhon (1974), Objective determination of the noise level in Doppler spectra, *J. Appl. Meteorol.*, *13*(7), 808–811, doi:10.1175/1520-0450(1974)013<0808:ODOTNL>2.0.CO;2.

Holland, J. Z., and E. M. Rasmusson (1973), Measurements of the atmospheric mass, energy, and momentum budgets over a 500-kilometer square of tropical ocean, *Mon. Weather Rev.*, *101*(1), 44–55, doi:10.1175/1520-0493(1973)101<0044:MOTAME>2.3.CO;2.

Kain, J. S., and J. M. Fritsch (1990), A one-dimensional entraining/detraining plume model and its application in convective parameterization, *J. Atmos. Sci.*, *47*(23), 2784–2802, doi:10.1175/1520-0469(1990)047<2784:AODEPM>2.0.CO;2.

Kollias, P., and B. Albrecht (2010), Vertical velocity statistics in fair-weather cumuli at the ARM TWP Nauru Climate Research Facility, *J. Clim.*, *23*(24), 6590–6604, doi:10.1175/2010JCLI3449.1.

Kollias, P., E. E. Clothiaux, M. A. Miller, B. A. Albrecht, G. L. Stephens, and T. P. Ackerman (2007), Millimeter-wavelength radars: New frontier in atmospheric cloud and precipitation research, *Bull. Am. Meteorol. Soc.*, *88*, 1608–1624, doi:10.1175/BAMS-88-10-1608.

Liu, Y., B. Geerts, M. Miller, P. Daum, and R. McGraw (2008), Threshold radar reflectivity for drizzling clouds, *Geophys. Res. Lett.*, *35*, L03807, doi:10.1029/2007GL031201.

Moran, K. P., B. E. Martner, M. J. Post, R. A. Kropfli, D. C. Welsh, and K. B. Widener (1998), An unattended cloud-profiling radar for use in climate research, *Bull. Am. Meteorol. Soc.*, *79*, 443–455, doi:10.1175/1520-0477(1998)079%3C0443:AUCPRF%3E2.0.CO;2.

Nicholls, S., M. A. Lemone, and G. Sommeria (1982), The simulation of a fair weather marine boundary layer in GATE using a three-dimensional model, *Q. J. R. Meteorol. Soc.*, *108*(455), doi:10.1002/qj.49710845510.

Norris, J. R. (1998), Low cloud type over the ocean from surface observations. Part II: Geographical and seasonal variations, *J. Clim.*, *11*, 383–403.

Nuijens, L., I. Serikov, L. Hirsch, K. Lonitz, and B. Stevens (2014), The distribution and variability of low-level cloud in the North Atlantic trades, *Q. J. R. Meteorol. Soc.*, *140*, 2364–2374, doi:10.1002/qj.2307.

Rauber, R. M., et al. (2007), Rain in shallow cumulus over the ocean: The RICO campaign, *Bull. Am. Meteorol. Soc.*, *88*(12), 1912–1928, doi:10.1175/BAMS-88-12-1912.

Siebesma, A. P., and J. W. M. Cuijpers (1995), Evaluation of parametric assumptions for shallow cumulus convection, *J. Atmos. Sci.*, *52*(6), 650–666.

Siebesma, A. P., and A. A. M. Holtslag (1996), Model impacts of entrainment and detrainment rates in shallow cumulus convection, *J. Atmos. Sci.*, *53*(16), 2354–2364, doi:10.1175/1520-0469(1996)053<2354:MIOEAD>2.0.CO;2.

Siebesma, A. P., et al. (2003), A large eddy simulation intercomparison study of shallow cumulus convection, *J. Atmos. Sci.*, *60*(10), 1201–1219, doi:10.1175/1520-0469(2003)60<1201:ALESIS>2.0.CO;2.

Stevens, B., et al. (2001), Simulations of trade wind cumuli under a strong inversion, *J. Atmos. Sci.*, *58*(14), 1870–1891, doi:10.1175/1520-0469(2001)058<1870:SOTWCU>2.0.CO;2.

Tiedtke, M. (1989), A comprehensive mass flux scheme for cumulus parameterization in large-scale models, *Mon. Weather Rev.*, *117*(8), 1779–1800, doi:10.1175/1520-0493(1989)117<1779:ACMFSF>2.0.CO;2.

Vali, G., R. D. Kelly, J. French, S. Haimov, D. Leon, R. E. McIntosh, and A. Pazmany (1998), Finescale structure and microphysics of coastal stratus, *J. Atmos. Sci.*, *55*(24), 3540–3564, doi:10.1175/1520-0469(1998)055<3540:FSAMOC>2.0.CO;2.

Wang, Y., and B. Geerts (2013), Composite vertical structure of vertical velocity in nonprecipitating cumulus clouds, *Mon. Weather Rev.*, *141*, 1673–1692, doi:10.1175/MWR-D-12-00047.1.

Warren, S. G., C. H. Hahn, J. London, R. M. Chervin, and R. L. Jenne (1988), Global distribution of total cloud cover and cloud type amounts over the ocean, *NCAR Tech. Note TN-317*.

Zhang, Y., and S. A. Klein (2013), Factors controlling the vertical extent of fair-weather shallow cumulus clouds over land: Investigation of diurnal-cycle observations collected at the ARM southern great plains site, *J. Atmos. Sci.*, *70*, 1297–1315, doi:10.1175/JAS-D-12-0131.1.